Astron. Astrophys. 323, 886–900 (1997)

ASTRONOMY
AND
ASTROPHYSICS

The influence of clumping on the infrared and radio continuum of early-type stars

R. Blomme and M. C. Runacres

Royal Observatory of Belgium, Ringlaan 3, B-1180 Brussel, Belgium

Received 25 April 1996 / Accepted 17 January 1997

Abstract. Time-dependent hydrodynamical models predict that the stellar winds of early-type stars are clumped, due to the sweeping up of material into dense shells. In this paper we investigate whether these shells can explain the long wavelength ($\geq$ 10 μm) continuum fluxes of O and early B stars. We had previously found that, for some stars, smooth wind models failed to explain the infrared and millimetre fluxes.

To calculate the continuum flux, we model the clumping by a single shell. This single shell can represent the joint effect of a number of shells and we discuss how multiple shells can be combined into a single shell. The shell strength parameter is introduced, which combines density contrast and width of the shell. From the 12, 25 and 60 μm IRAS observations of ζ Pup, we derive a shell strength and position. We find that the clumping is less extreme than predicted by the hydrodynamical models. This means that the strength of the shells is less than the models predict, that there are not as many of them or that they do not fill a complete solid angle.

Considering such *partial* (i.e. filling a solid angle of $< 4\pi$) shells is a natural way to make the time-dependent hydrodynamical models agree with the observations. That *complete* shells are found in the hydrodynamical models is solely a consequence of present computational limitations. When we introduce partial shells in our model for ζ Pup, we find that the IRAS observations can be explained if each shell is limited to a solid angle of $\sim 4\pi/3$.

The shells dissipate as they move away from the star, but reach the radio formation region before they damp out completely, thereby influencing the radio fluxes of the stars. In this case, applying a *smooth* wind model to the radio observations of an O or early B star could lead to an overestimate of the mass loss rate. In the case of ζ Pup this error turns out to be negligible.

While clumping can explain the observed infrared continuum fluxes of O and early B stars, it cannot be excluded that other phenomena also contribute. Co-rotating interaction regions especially will influence the infrared flux formed in the wind.

Key words: stars: atmospheres – stars: early-type – stars: mass loss – infrared: stars – radio continuum: stars

Send offprint requests to: M. Runacres

1. Introduction

The stellar winds of O and B stars are generally thought to be driven by the star's radiation. Momentum is transferred from the radiation field to the material in the wind by absorption in spectral lines. The theory of radiatively driven winds was first proposed by Lucy & Solomon (1970) and was further developed by i.a. Castor et al. (1975) and Pauldrach et al. (1986, 1994). Although Lucy & Solomon already realized that the driving mechanism is inherently unstable, the standard models treat the wind as a steady, smooth and spherically symmetric outflow and predict mass loss rates ($\dot{M}$) and terminal velocities (v_∞) that agree with the observations reasonably well (Groenewegen et al. 1989; Blomme 1990; Lamers & Leitherer 1993; Puls et al. 1996).

However, observational features that are incompatible with such a smooth stellar wind can be found in every wavelength region. A smooth wind is not expected to have gas hot enough to generate a detectable amount of X-rays. Yet all O and early B stars which are sufficiently close by to be detected have an X-ray luminosity of approximately 10^{-7} of their bolometric luminosity, suggesting that part of the wind has an unexpectedly high temperature (Pallavicini et al. 1981; Chlebowski 1989; Sciortino et al. 1990). The existence of high temperature regions is also inferred from the superionization of oxygen (MacFarlane et al. 1993). Variability in X-ray emission has been detected for a few stars (Snow et al. 1981; Cassinelli et al. 1983; Collura et al. 1989; Berghöfer & Schmitt 1994).

In the ultraviolet, the P Cygni profiles of *unsaturated* lines show variability in the form of Discrete Absorption Components (DACs). These are opacity enhancements in the absorption trough of the profile, appearing at a velocity of $\sim 0.3v_\infty$ and moving blueward up to v_∞. This happens on time-scales which are closely connected with the rotation period of the star (Prinja 1988; Kaper et al. 1996). Probably related to the DACs are the variations in the edge velocity (e.g. Lamers et al. 1988; Kaper et al. 1996). The very dark and broad absorption troughs (so called "black troughs") of *saturated* P Cygni profiles are another observational feature that is unexpected for a smooth wind (Lucy 1982, 1983). Equally unexpected is the high "tur-

bulence" (100 – 300 km s^{-1}) needed to obtain a good fit of the observed P Cygni profiles (Groenewegen & Lamers 1989).

For many stars the Hα emission line is also variable on a time-scale connected with the rotation period of the star (e.g. Conti & Frost 1977; Ebbets 1980, 1981, 1982; Rusconi et al. 1980; Snow et al. 1980; Moffat & Michaud 1981; Olson & Ebbets 1981). For the O 4 If star ζ Pup, this time-scale has also been found in the X-ray variability (Berghöfer et al. 1996). For the same star, linear spectropolarimetry of Hα (Harries & Howarth 1996) suggests that the density of the stellar wind is enhanced toward the equatorial plane.

Abbott et al. (1984a) obtained 2 to 20 μm observations of 16 early-type stars and compared them with model fluxes from Castor & Simon (1983). They adopted a standard β velocity law with $\beta = 1$ and found that, for most stars, the observations exceed the model. This was seen as an indication that the wind accelerates more gradually than predicted by a $\beta = 1$ law. Runacres & Blomme (1996, hereafter Paper I) found that the observed infrared and millimetre fluxes of a number of O and B stars are larger than expected from a smooth wind. In the radio region, Abbott et al. (1984b) and Bieging et al. (1989) found a number of O stars to have non-thermal emission. These stars show considerable variability in their radio emission or a slope of the continuum that is not compatible with a thermal source.

All these observations suggest a more subtle and complex picture of a stellar wind, where average properties may well be described by that of a smooth wind model, but where deviations from a steady, smooth and spherically symmetric outflow are important. Most notably, considerable structure should be present in the stellar wind, making it *clumped* rather than smooth, and part of the wind should be hot ($\sim 10^6$ K).

It is useful to distinguish between structure on a relatively large scale and structure on a smaller scale (Owocki 1994a,b). The small scale structure would be caused by shocks due to the inherent instability of the radiative driving mechanism (Lucy & Solomon 1970; Lucy 1984; Owocki & Rybicki 1984, 1985, 1986; Rybicki et al. 1990). Time-dependent hydrodynamical calculations confirm that shocks develop and persist in the wind (Owocki et al. 1988; Owocki 1994a; Feldmeier 1995). These models picture the wind as a sequence of slow dense shells – bounded by a strong reverse shock on the inside and a weaker forward shock on the outside – with fast low density material between the shells. The shocks heat part of the material, which can explain the observed X-ray fluxes (e.g. for ζ Pup, see Hillier et al. 1993). Through Auger ionization close to the stellar surface these X-rays can produce the superionized O VI (MacFarlane et al. 1993). The non-monotonic velocity law of the time-dependent models would increase the efficiency with which radiation from the star is absorbed and could thus explain the black absorption troughs of saturated P Cygni profiles. The velocity changes across the shocks could also explain the high turbulent velocities which are found in fitting the ultraviolet P Cygni profiles.

The large scale structure might consist of co-rotating interaction regions (CIRs). CIRs are a consequence of the collision between slower and faster moving material in the rotating wind (Mullan 1984, 1986; Cranmer & Owocki 1996). The difference in velocity could be due to magnetic fields rooted in the photosphere, or non-radial pulsations. Magnetic fields below the current detection limits are estimated to be sufficient (Owocki 1994a,b). These CIRs could explain the correlation of the variability time-scales of the ultraviolet P Cygni profiles and Hα with the rotation period of the star. The combination of magnetic fields and shocks (far out in the wind) can also explain the non-thermal radio emission (White 1985).

Shocks can also be the result of the interaction of the smooth wind with a wind-compressed disk (Cassinelli et al. 1994). Bjorkmann & Cassinelli (1993) first proposed that rapid stellar rotation compresses the material of the stellar wind toward the equatorial plane, giving rise to a wind-compressed zone or disk. Petrenz & Puls (1996) found that even rotational velocities well below those needed to form a disk increase the emission in Hα through the so called ρ^2-effect. This could well explain the results found in the linear spectropolarimetry of Hα in ζ Pup (Harries & Howarth 1996). Recently, the wind-compressed disk hypothesis has been challenged by Owocki et al. (1996) who claim that nonradial line-forces can inhibit the formation of such a structure.

The present work focuses on the infrared and radio continuum of O and B stars. Since the free-bound and the free-free emission that form the long wavelength continuum are proportional to the square of the density, density contrasts should be easy to detect. An advantage of studying the continuum rather than lines is that complications due to the non-monotonic velocity structure do not arise, making the modelling and interpretation easier.

Lamers & Waters (1984) studied the influence of clumps and hot blobs on the infrared and radio continuum using their curve of growth method. They derived a number of expressions for the effect of clumping on the flux. However, they assume the typical size of a clump to be much smaller than the mean free path of a photon. Such clumping is therefore substantially smaller than the small scale structure referred to by Owocki (1994a,b). The wind has to contain a large number of such clumps for any effect on the flux to be seen. Owocki (1992) presented the infrared flux for a clumped model of ζ Pup, using the density structure from his time-dependent hydrodynamical calculations. He found the flux to be too strongly enhanced by the shells to be able to fit the observations. A model with a smaller perturbation at the base of the wind would produce a better fit. Runacres & Blomme (1994) calculated the emergent flux for a phenomenological model of the density structure based on Owocki's calculations but with the shells damping out between 5 and 10 stellar radii (R_*) and a smooth wind beyond that. They found an emergent flux which was only slightly higher than the observations.

In Paper I we applied a NLTE model of a time-independent, spherically symmetric and smooth wind to a sample of 18 O and early B stars (up to B 3). We used the observed visual and near infrared magnitudes to determine distance and interstellar extinction, and the observed radio fluxes to determine the mass loss rate, leaving the far infrared and millimetre continuum unconstrained. We found discrepancies between the model and the

observations in the 25 μm - 1.3 mm range for four stars in the sample. In Paper I discrepancies were only judged significant if they occurred in various independent observations and were large compared to the general scatter of the observations. Because of this conservative approach and the lack of observations beyond 12 μm for many stars in our sample, the fraction of discrepant stars is *not* to be regarded as a statement in a statistical sense of how common clumping is among O and B stars.

In the present paper we model clumping by complete or partial (i.e. filling a solid angle $< 4\pi$) shells. We base our values of the position, density contrast and width of the shells on the values from the time-dependent hydrodynamical models of Owocki and of Feldmeier. We simplify somewhat the results found in the time-dependent calculations, for reasons of conceptual and computational simplicity. We construct our shells by taking acceptable values of shell density contrast and width from the detailed calculations. Both may vary as a function of distance. To make comparisons meaningful, we ensure that the smooth models and the clumped models contain the same mass. In most of our modelling we shall study the influence of a single shell. Nevertheless useful results and conclusions will be derived for multiple shells as well. The important point is that the shells we study represent either the effect of a single shell, as modelled, or the combined effect of a number of shells. Simple estimates of how multiple shells combine into a single shell will be given. Even clumps of a more stochastic nature can be combined into a single (partial) shell. The detailed study of such clumping will be the subject of a subsequent paper.

In Sect. 2 we introduce our numerical model for complete shells together with some analytical simplifications. In Sect. 3 we compare the model results to the observations. The wealth of large wavelength observations for ζ Pup allows us to determine the size and the positions of the shells that can explain the discrepancies found in Paper I. For the other stars, the shell dimensions are not always well-constrained. The Owocki and Feldmeier models overestimate the ζ Pup infrared fluxes, a situation we try to remedy in Sect. 4 by introducing *partial* shells. In Sect. 5 we discuss the results. Conclusions are presented in Sect. 6.

2. Complete shells

2.1. Numerical models

The free-free and the free-bound emission that form the infrared and radio continuum are proportional to the square of the density (ρ). The velocity due to shocks in the material is not relevant as the continuum processes are not influenced by it. The density was derived from the time-dependent hydrodynamical calculations by Owocki and collaborators (Owocki et al. 1988; Owocki 1992, 1994a) and Feldmeier (1995). In those models most of the stellar wind material is concentrated in narrow, high density shells. We use the published snapshots of the density to derive typical values for the shell parameters.

The geometric width of a single shell ($\Delta R_{\rm sh}$) is typically about 0.05 – 0.2 R_*, where the larger value is more appropriate at larger distances from the star ($\sim 10R_*$). The density contrast with respect to the *smooth* wind ($\rho_{\rm sh}/\rho_0$) is typically 50 close to the star, decreasing to ~ 5 further out. Between $1-5R_*$ there are some $10-15$ shells.

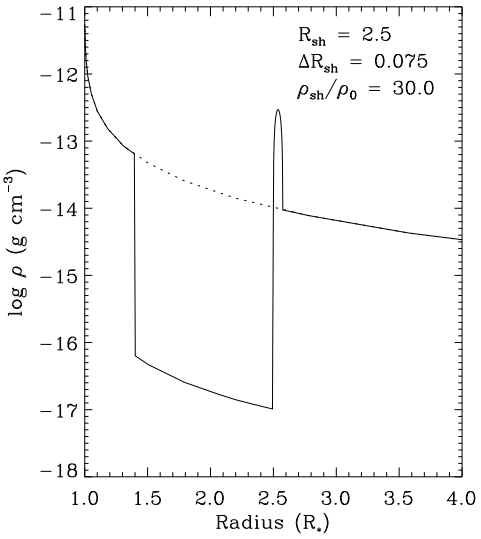

Fig. 1. The density (ρ) of a single shell and corresponding trough as a function of radius (full line). The dashed line shows the smooth wind. The mass of the material in the shell is compensated exactly by the mass taken out by the trough

The temperature in the wind will increase considerably due to the presence of shocks. However, either the geometric extent over which this happens is low (for shells close to the star), or the density of the material where it happens is low (for shells at large distances from the star – see Feldmeier 1995, his Figs. 10 and 12). We therefore do not expect much influence of the temperature on the infrared and radio emission. We simply take the temperature of the material in the shell to be the same as the material in the wind. This assumption will be discussed in detail in Sect. 5.2.

In constructing numerical models we use the code described in Paper I. The density of the *smooth* wind used in this code is calculated using the k, α and δ formalism (Pauldrach et al. 1986). In order to introduce, at a position $R_{\rm sh}$, a single shell-like inhomogeneity with a width $\Delta R_{\rm sh}$, we define the density of the inhomogeneous wind in the following way: between $R_{\rm sh}$ and $R_{\rm sh} + \Delta R_{\rm sh}$ we have

$$\rho(r) = \rho_{\rm smooth}(r) \left\{ 1 + \left(\frac{\rho_{\rm sh}}{\rho_0} - 1 \right) \left(1 - \left(\frac{r - (R_{\rm sh} + \Delta R_{\rm sh}/2)}{\Delta R_{\rm sh}/2} \right)^2 \right) \right\} \quad (1)$$

where $\rho_{\rm sh}/\rho_0$ is the density contrast with respect to the smooth wind. Elsewhere, $\rho(r) = \rho_{\rm smooth}(r)$. This means that we add a parabolic peak to the density. Note that in this paper, values for $\Delta R_{\rm sh}$ will always be expressed in R_*, while $\rho_{\rm sh}/\rho_0$ is of course unitless. The shell covers the complete solid angle of 4π.

An important principle in the construction of our models is that the mass contained in them should be the same as for the smooth wind in order to make comparisons meaningful. To ensure this, we introduce a trough on the inner side of the peak. The size of the trough is such that the mass of the matter "taken away" from the wind in the trough exactly compensates the matter "added" in the peak. A typical example of such a shell is shown in Fig. 1. The density in the trough is taken to be $10^{-3}\rho_{\rm smooth}$. This picture is consistent with the one derived from the time-dependent hydrodynamical models, where fast sparse matter collides with a slower dense layer. If needed, the procedure described above can be repeated at will to introduce an arbitrary number of shells in the wind. Note that the distance between two shells is constrained by the width of the troughs. For the shell shown in Fig. 1 the inclusion of the trough in the density reduces the emergent radiative flux of the model by 5 % compared to a model with only a peak. For a sequence of 10 such shells between 1 and 20 R_* the effect on the flux of either including the troughs or not is also about 5 %.

Contrary to Paper I we do not solve the equations of statistical equilibrium and radiative transfer self-consistently. This could in principle be done, but the correct description of a shell drastically increases the number of points in the depth grid and the computation time of a model is roughly cubically proportional to the number of these points. Therefore, since a large number of models must be calculated covering the full range of possible shell positions, widths and density contrasts, iterating a consistent NLTE model to convergence for every combination of these parameters would have been too costly in computer time. Instead, we have opted for a simplified approach. First a consistent NLTE model for a smooth wind is calculated using the temperature law from Bunn & Drew (1992). Based on this model a "pseudo-NLTE" model is calculated by adapting the temperature law until the LTE flux from the model with the modified temperature law agrees with the emergent flux from the NLTE model (to within 5 %). The modified temperature is about $20 - 30$ % higher than the original law, except close to the stellar surface. The clumped models are then calculated using the temperature law modified in this manner. We verified the validity of this approach by comparing with a fully iterated model of a clumped wind. The comparison showed the error introduced by this approach to be less than 20 %. This error does not change the general nature of our conclusions, as we only wish to investigate whether shells can explain the observed infrared and millimetre fluxes and what kind of shell parameters we derive for sufficiently well-observed stars. Moreover, once the shell parameters have been constrained in pseudo-NLTE, a small grid of true NLTE models can easily be calculated to provide more accurate quantitative results, if needed.

For the ionization and excitation structure given by the pseudo-NLTE model, the radiative transfer equations are solved for a grid of wavelengths, using the improved Feautrier technique developed by Rybicki & Hummer (1991). As a lower boundary condition we use a photospheric model calculated with the Hubeny (1988) code (see Paper I). The atomic data for hydrogen and helium are as in Paper I. For the stars we study, all stellar parameters, stellar wind parameters and interstellar extinction are also as in Paper I. The final part of the model consists of calculating the flux, by integrating the emergent intensity over impact parameter, using a trapezoidal integration method.

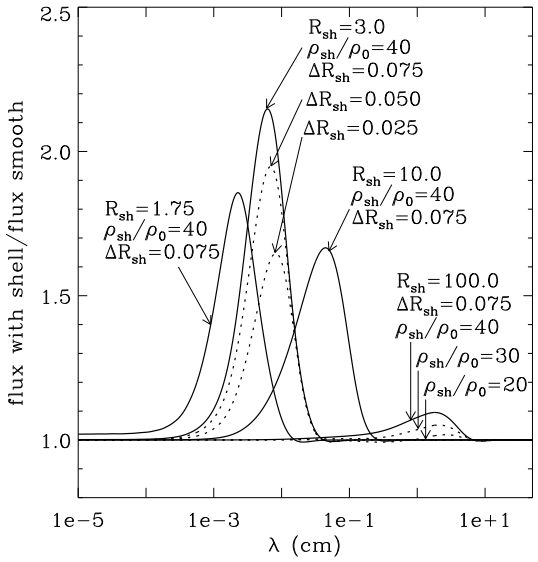

Fig. 2. Some typical results, where the differential effect on the flux is plotted as the ratio of the flux of the wind model with a single shell to the flux of the equivalent smooth wind model. The full line graphs show the effect of shell position ($R_{\rm sh}$), while the dashed line graphs illustrate the effect of width ($\Delta R_{\rm sh}$) and density contrast ($\rho_{\rm sh}/\rho_0$)

Fig. 2 shows the differential effect on the flux of the wind model with a shell (with respect to the flux of the equivalent smooth wind) as a function of wavelength for some typical examples. Note how the effect of a given shell structure (width and contrast) first increases as the shell moves out and then goes down as the shell continues to move further out.

2.2. Analytical simplifications

Some interesting results can be derived from a more simplified version of the problem, inspired by the work of Wright & Barlow (1975). They calculated the infrared and radio flux due to free-free emission for a smooth (time-independent) stellar wind, assuming spherical symmetry, a density falling off as r^{-2} and ionization proportional to the density. In this simplification, the number density of ions (N) is given by:

$$N = \left(\frac{\dot{M}}{4\pi\mu m_{\rm H} v_\infty}\right)\frac{1}{r^2} =: \frac{A}{r^2} \qquad (2)$$

where $\dot{M}$ is the mass loss rate, v_∞ the terminal velocity in the wind, μ is the mean atomic weight and $m_{\rm H}$ the mass of the hydrogen atom. The free-free opacity (which is the main opacity contributor at large wavelengths) is given by:

$$\chi = n_{\rm e} N K(\lambda, T) = \gamma N^2 K(\lambda, T) \qquad (3)$$

where γ is the ratio of electron density to ion density and

$$K(\lambda, T_{\rm w}) = 3.7 \times 10^8 \left\{1 - \exp\left(-\frac{hc}{kT_{\rm w}\lambda}\right)\right\} \times g(\lambda, T_{\rm w}) Z^2 T_{\rm w}^{-0.5} \left(\frac{\lambda}{c}\right)^3 \quad (4)$$

where λ is the wavelength, $T_{\rm w}$ the temperature in the wind, Z^2 is the average square charge and $g(\lambda, T_{\rm w})$ the average Gaunt factor. For the sake of simplicity, in this section we approximate the shape of the shell by a rectangle instead of the parabolic law of Eq. (1).

Along each impact parameter p we can calculate the total optical depth in the wind ($\tau_{\rm max}$), which consists of two parts: the total optical depth in the *smooth* wind and the additional effect due to the *shell* ($\tau_{\rm add}$). We neglect the presence of a trough, as its effect is small (see Sect. 2.1). In the simplifying assumptions we use in this section, the wind and shell are assumed to be isothermal. The formal solution for the emergent intensity can therefore be integrated analytically. The flux is then obtained by integration of the emergent intensity (multiplied by p) over the impact parameters.

For a shell at a given distance $R_{\rm sh}$, the additional optical depth $\tau_{\rm add}$, at each impact parameter p, will depend on $\rho_{\rm sh}/\rho_0$ and $\Delta R_{\rm sh}$. Depending on the number of times the impact parameter crosses the shell, we can write $\tau_{\rm add}(p) = \tau_{\rm one}$ ($p < R_*$) or $\tau_{\rm add}(p) = 2\tau_{\rm one}$ ($p \geq R_*$), where we can approximate:

$$\tau_{\rm one}(p) := \int_{r=R_{\rm sh}}^{r=R_{\rm sh}+\Delta R_{\rm sh}} \chi_{\rm add}(p, z) {\rm d}z \approx \gamma N_{\rm smooth}^2(R_{\rm sh}) K(\lambda, T_{\rm w}) \frac{\Delta z}{\Delta R_{\rm sh}} \times \left(\left(\frac{\rho_{\rm sh}}{\rho_0}\right)^2 - 1\right) \Delta R_{\rm sh} \quad (5)$$

where $N_{\rm smooth}$ is the number density of the ions in the smooth wind and $\Delta z/\Delta R_{\rm sh}$ is a geometric factor due to the impact parameter not necessarily crossing the shell radially. We have used the fact that the opacity is proportional to ρ^2 [Eq. (3)].

For a given $R_{\rm sh}$ the geometric factor $\Delta z/\Delta R_{\rm sh}$ is quite insensitive to the value of $\Delta R_{\rm sh}$. As long as the combination of $\rho_{\rm sh}/\rho_0$ and $\Delta R_{\rm sh}$ gives the same $((\rho_{\rm sh}/\rho_0)^2 - 1)\ \Delta R_{\rm sh}$, the same $\tau_{\rm add}$ will result. This will result in the same emergent intensity and the same flux. In view of the density contrasts expected we can drop the -1 term and introduce a parameter which we shall call the shell strength ($f_{\rm sh}$):

$$f_{\rm sh} := \rho_{\rm sh}/\rho_0 . \Delta R_{\rm sh}^{0.5}. \quad (6)$$

As usual, $\Delta R_{\rm sh}$ is expressed in units of R_* and $\rho_{\rm sh}/\rho_0$ is unitless. The important point is that *shells at the same position ($R_{\rm sh}$) with the same shell strength ($f_{\rm sh}$) will have the same differential effect on the flux*. This relation is very useful as it allows us to reduce the number of parameters we have to study. It also means that, when applying models to the observations, only information about $f_{\rm sh}$ can be derived, no separate information about $\rho_{\rm sh}/\rho_0$ and $\Delta R_{\rm sh}$ is possible.

The shell strength might be expected to lose its significance for shells with a very large density contrast. In that case, the optical depth across the shell becomes so large that an external observer only sees the radiation coming from the outer part of the shell. Therefore, only the outer part of the geometrical width $\Delta R_{\rm sh}$ plays a role and the arguments on which the derivation of the shell strength was based, no longer hold. However, for such large values of the optical depth, the flux is close to its saturation value (see Sect. 2.3), and it is of little consequence whether the total width of the shell contributes to the flux, or only the outer part of it. The basic idea that shells with the same $f_{\rm sh}$ have the same effect on the flux remains valid over a large range of $f_{\rm sh}$. The small differences due the $\Delta R_{\rm sh}$ problem are expected to be largest close to the stellar surface (where $\Delta R_{\rm sh}$ is a larger fraction of $R_{\rm sh}$). Numerical calculations show that the differences in flux between a $0.1R_*$ and a $0.01R_*$ shell are 15% for $R_{\rm sh} = 1.1R_*$, falling below 10% for $R_{\rm sh} = 2.0R_*$ and below 1% for $R_{\rm sh} = 15R_*$.

In the application of our detailed models to observations, we always introduce a shell by specifying its density contrast and width. Only for the figures do we combine these into the shell strength. This allows us to see how good a parameter the shell strength is.

Equation (6) was derived solely from reasoning about $\tau_{\rm add}$. In the integration over the impact parameters (to derive the flux), changes in $\Delta R_{\rm sh}$ will result in certain impact parameters p no longer crossing the shell. This will also change the resulting flux. This shows that Eq. (6) is only an approximation, though a reasonably good one.

Wright and Barlow (1975) introduced the concept of an effective radius. In a very simplified picture of the situation this is the radius where the radiation at a particular wavelength is formed. In reality, most of the radiation comes from a more extended formation region. The idea of a formation region is important because it allows us to link the flux at a given wavelength with a geometrical region in the wind. For a smooth wind with parameter values typical for ζ Pup, the extent of the formation region is given in Table 1. We can introduce such an effective radius in the present model as well, but its definition will also depend on the parameters of the shell. We are interested specifically in where we have to position the shell ($R_{\rm sh}$) to get the maximum differential effect on the flux at a certain wavelength $\lambda_{\rm max}$. An expression for $\lambda_{\rm max}$ is derived in Appendix A.

Another conclusion that can be derived from these simple models is that the *maximum* differential effect on the flux (as a function of λ) is independent of the mass loss rate of the smooth wind. This is because, ultimately, the maximum effect depends on the behaviour of the total optical depth ($\tau_{\rm max}$) as a function of p. For a smooth wind $\tau_{\rm max}$ is proportional to $K\gamma A^2$ (Wright & Barlow 1975). Similarly, the additional optical depth ($\tau_{\rm add}$) due to the shell can always be written as $K\gamma A^2$ multiplied by a geometrical factor which is the result of the integration over z. Thus any combination of $K\gamma A^2$ that gives the same $\tau_{\rm max}$ (for all p) will result in the same maximum differential effect.

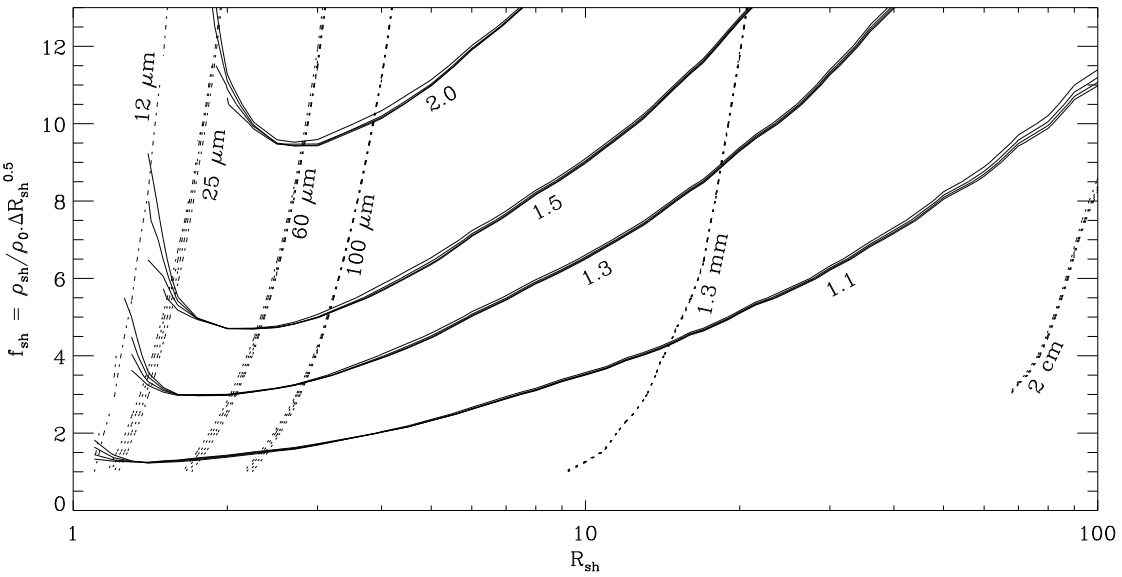

Fig. 3. Effect of a *single* shell on the continuum flux of ζ Pup. Full line: contour levels of the maximum differential effect as a function of shell position ($R_{\rm sh}$) and shell strength ($f_{\rm sh}$), which combines both the shell contrast and width. Dashed line: the wavelength ($\lambda_{\rm max}$) at which the maximum effect occurs. The quadruplets of lines give the results for 4 values of $\Delta R_{\rm sh}$, which allows one to judge the accuracy of Eq. (6). The curves for the maximum effect are independent of mass loss rate, terminal velocity, abundance, γ, temperature and Gaunt factor. The wavelength ($\lambda_{\rm max}$) *does* depend on these factors however. The 2 cm curve is cut off when absorption starts to dominate at low $f_{\rm sh}$ values

Table 1. Extent of the formation region of the flux at various wavelengths. The formation region at a certain wavelength is here defined as the range where 80 % of the total flux emitted in the *wind* comes from. A smooth wind with parameters typical for ζ Pup (see Paper I) has been used. These values change somewhat when a shell is included (Appendix A) and can change considerably when a partial shell is present (Sect. 4.2). Besides the wavelengths studied here, we also give wavelengths for some of the Infrared Space Observatory (ISO) filters

λ	extent (R_*)			λ	extent (R_*)		
12 μm	1	-	1.5	160 μm	1.6	-	14
25 μm	1	-	3	1.3 mm	3	-	60
60 μm	1	-	7	2 cm	25	-	450
90 μm	1	-	10	6 cm	50	-	900

Changing the mass loss rate changes A^2, but this is compensated for by the change in K, i.e. in λ. So, exactly the same value for the maximum effect is found, but at a different wavelength. Similarly, the maximum differential effect is independent of v_∞, abundance, γ, temperature and the value for the Gaunt factor.

A single shell from our models may well represent the combined effect of a number of shells. Under the simplifying assumptions of this section it is easy to derive how different "sub-shells" combine into a single shell. The set of sub-shells will produce the same effect at a given wavelength if their optical depths add up to the same optical depth as the single shell. Care must be taken that the sub-shells are in the same formation region as the original shell.

In what follows, $f_{\rm sh}$ denotes the strength of the single shell. Assume that n identical sub-shells with $\rho_{\rm sub}/\rho_0$ and $\Delta R_{\rm sub}$ produce the same effect on the flux as the single shell. From the constraint that these should add up to the same $\tau_{\rm add}$ and Eq. (6), we find:

$$n \left(\frac{\rho_{\rm sub}}{\rho_0} \right)^2 \Delta R_{\rm sub} = f_{\rm sh}^2. \qquad (7)$$

If we assume that the shape of the trough is rectangular, that in the trough *all* material is removed to compensate for the sub-shell and that the density goes as r^{-2}, one can show that the width of a single trough ($\Delta R_{\rm tr}$) is given by $(\rho_{\rm sub}/\rho_0 - 1)\Delta R_{\rm sub}$. If we allow sub-shells to exist over a total range in radius of $D_{\rm sub}$ then we have $n(\Delta R_{\rm sub} + \Delta R_{\rm tr}) = D_{\rm sub}$. After some calculation this gives:

$$D_{\rm sub} = \frac{f_{\rm sh}^2}{(\rho_{\rm sub}/\rho_0)}. \qquad (8)$$

$D_{\rm sub}$ should be comparable to the size of the formation region of the given wavelength. The density contrast and the width of the n sub-shells are then given by Eqs. (7) and (8). Note that n is a free parameter, so that even a very large number of weak sub-shells are possible. Inverting the above line of reasoning, we see that a large number of shells can be swept up into a single shell with the same effect on the flux. Of course, one can only sweep up shells within the formation region of the wavelength under consideration.

2.3. Results

We now leave the analytical models and turn to the more detailed computer models. We calculated a grid of models for typical parameter values of ζ Pup. We determined the maximum differential effect and its corresponding wavelength $\lambda_{\rm max}$ for a grid of $\rho_{\rm sh}/\rho_0$ and $\Delta R_{\rm sh}$ values, at different $R_{\rm sh}$ values. We plot the results of our grid in Fig. 3, where we show contour levels of the maximum differential effect as a function of the position of the shell ($R_{\rm sh}$) and the shell strength ($f_{\rm sh}$). The quadruplets of lines give the results for four values of $\Delta R_{\rm sh}$. The spread in these lines allows one to judge the accuracy of combining $\rho_{\rm sh}/\rho_0$ and $\Delta R_{\rm sh}$ into a single shell strength $f_{\rm sh}$, given by Eq. (6). The good agreement shows that, also in the numerical models, the number of parameters describing the shell can be reduced by introducing the shell strength.

Also indicated on Fig. 3 are the contour levels for $\lambda_{\rm max}$, i.e. the combinations of $R_{\rm sh}$ and $f_{\rm sh}$ that give a certain value for $\lambda_{\rm max}$. The contour lines of $\lambda_{\rm max}$ are nearly vertical, showing that there is an almost one-to-one relation between geometric depth in the wind and wavelength of maximum effect. This shows that the concept of a formation region is still valid here.

Close to the stellar surface, no shells are possible because insufficient material remains between the shell and the stellar surface to form the corresponding trough. At small radii, the contour lines of the maximum effect go to high values. This is the result of a saturation effect. A shell with a very high shell strength will emit a flux proportional to $4\pi(R_{\rm sh}+\Delta R_{\rm sh})^2 B(\lambda, T_{\rm w})$, compared to the $4\pi R_*^2 B(\lambda, T_*)$ emitted by the star itself (where we neglect the smooth wind to keep the discussion simple). If the shell and star are at the same temperature, the maximum effect can therefore never be higher than $(R_{\rm sh}+\Delta R_{\rm sh})^2/R_*^2$. Close to the stellar surface, high $f_{\rm sh}$ values are needed to obtain even a small maximum differential effect.

Fig. 3 can be used as a more accurate method of linking $R_{\rm sh}$, $\rho_{\rm sh}/\rho_0$, $\Delta R_{\rm sh}$ and $\lambda_{\rm max}$ than the formula derived in Appendix A. The figure can also be used as a first step in deriving information from observations, by converting observed (maximum) effects at a given wavelength to shell position and strength. When applying this figure to other stars than ζ Pup, one must note that contrary to the maximum differential effect, the $\lambda_{\rm max}$ value *is* sensitive to various parameters ($\dot{M}$, v_∞, etc.). For stars with smaller $\dot{M}$, the effect of clumping will be seen at larger wavelengths. The conversion factor can be derived from Eq. (A6). As one cannot know whether an observed effect is a maximum effect, we prefer to use our more detailed models in the following section.

3. Application to observations

We present the techniques we use in detail for ζ Pup (HD 66811, O 4 If) since this is the best-observed star from our sample (see Paper I). The far infrared observations we use are the filter-integrated 12, 25 μm observations from the IRAS Point Source Catalog (Beichman et al. 1988) and, since the Point Source Catalog only gives an upper limit for 60 μm, the monochromatic 60 μm flux from Lamers et al. (1984). We also include the monochromatic 1.3 mm flux from Leitherer & Robert (1991). For ζ Pup and a number of other stars, the discrepancies between the observations and the *smooth* stellar wind model (as derived from Paper I) are summarized in Table 2. The observations at 60 μm will allow us to put stronger constraints on the shell parameters than can be done for the other stars, for which no such observations are available.

Using the model described in Sect. 2.1, we try to answer the following three questions:

- can single or multiple shells explain the discrepancies we found between the smooth wind theory and the observations?
- do the observations allow us to determine the position, strength and number of shells?
- do the position, strength and number of shells agree with the predictions of the time-dependent hydrodynamical models?

First we calculate the emergent fluxes for a grid of models with a *single* shell, with different position, density contrast and width. We correct the emergent fluxes for interstellar extinction in the same way as in Paper I and then integrate them for the 12 and 25 μm filters. The density contrast and width are combined into the shell strength parameter [Eq. (6)] Then, we draw the contour lines for the differential effects on the flux at the different wavelengths (Fig. 4). The values we choose for the contour levels are the discrepancies found between the observations and the *smooth* wind model. When including the error bars, this gives us three lines for each wavelength.

Not to overburden Fig. 4, only the $\Delta R_{\rm sh}$ = 0.025 result is presented. We checked that shells with the same shell strength give the same effect on the flux: the other $\Delta R_{\rm sh}$ values give very similar results. A rather low value for $\Delta R_{\rm sh}$ has been taken to allow shells to be placed as close as possible to the star. The vertical asymptotes for small values of $R_{\rm sh}$ can be explained by the saturation effect described in Sect. 2.3.

It is useful to be able to summarize this region by specifying a central point and a range in $R_{\rm sh}$ and $f_{\rm sh}$. For most of the discussion it is not necessary to take into account the detailed shape of the region. The central point is taken as the centre of mass of the region. The range in $R_{\rm sh}$ is simply determined by the minimum and maximum values of the region and the same is applied for $f_{\rm sh}$.

Fig. 4 shows that a shell at 2 stellar radii with a shell strength of $\sim$ 7.5 (e.g. $\Delta R_{\rm sh} \approx 0.1 R_*$ and $\rho_{\rm sh}/\rho_0 \approx 25$) can reproduce the observed effect at the IRAS wavelengths. It is clear from the same figure that this single shell *cannot* explain the 1.3 mm discrepancy. At least one more shell at larger distances ($\sim 10 - 30\ R_*$) must be present. A shell at this distance from the star has no influence on the fluxes at the IRAS wavelengths, which justifies the independent treatment of the two wavelength regions.

It is interesting to note that MacFarlane et al. (1993), in their study of the observed superionization of O VI, conclude that strong shocks must begin forming at $r \lesssim 2\ R_*$ in order to produce the X-rays to ionize oxygen. These shocks could be

Table 2. Ratio between observations and *smooth* model fluxes for a number of stars. The model fluxes have been integrated over the corresponding filters for 12, 20 and 25 μm. They are monochromatic for 60 μm and 1.3 mm

	$F_{\rm obs}/F_{\rm smooth}$					
λ	HD 66811 (ζ Pup)	HD 15570	HD 30614 (α Cam)	HD 36486 (δ Ori A)	HD 38771 (κ Ori)	HD 210839 (λ Cep)
12 μm	1.18 $\pm$0.05	-	1.10 $\pm$0.07	1.14 $\pm$0.04	1.22 $\pm$0.05	0.97 $\pm$0.21
20 μm	-	2.77 $\pm$0.88	-	-	-	1.18 $\pm$0.15
25 μm	1.58 $\pm$0.10	-	1.31 $\pm$0.19	1.27 $\pm$0.10	1.34 $\pm$0.11	-
60 μm	1.46 $\pm$0.23	-	-	-	-	-
1.3 mm	1.35 $\pm$0.12	-	-	-	-	-

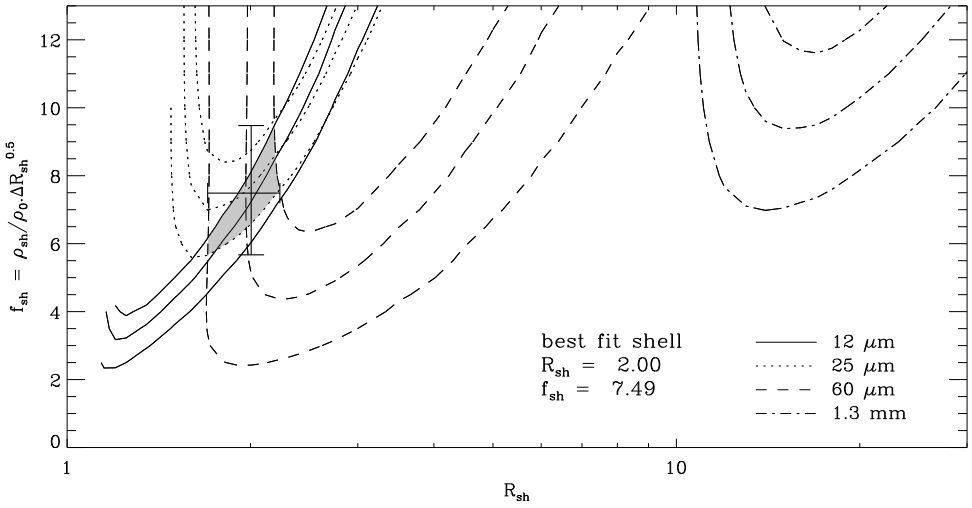

Fig. 4. Contour plot for ζ Pup showing the differential effect of a *single* shell on the flux. $R_{\rm sh}$ and $\Delta R_{\rm sh}$ are in units of R_* and $\rho_{\rm sh}/\rho_0$ is unitless. The region indicated by the full lines gives all combinations of $R_{\rm sh}$ and $f_{\rm sh}$ that can explain the 12 μm discrepancy. The middle full line gives the best value for this discrepancy, the outer full lines give the error bars. The other lines indicate the combinations of $R_{\rm sh}$ and $f_{\rm sh}$ needed to explain the 25, 60 μm and 1.3 mm discrepancies. The shaded area shows the possibilities for the single shell that can explain all IRAS discrepancies (but not the 1.3 mm one). The best fit solution is indicated by the cross in the centre of the shaded area, while its size gives the error bars on $R_{\rm sh}$ and $f_{\rm sh}$

associated with the shells studied here, and the positions we find are therefore consistent with the MacFarlane et al. results.

The *single* shell we find has a strength similar to those of the time-dependent hydrodynamical models. However, in these models there are *many* shells. More likely than not, our single shell actually represents the effect of a number of shells in the same formation region, but which are *weaker* than the theoretical predictions. This discrepancy can be resolved if:

- the real shells are weaker than predicted
- the predicted shells have the right strength, but there are less of them
- both the strength and number of shells agree with the predictions, but the shells do not fill a complete solid angle.

Weaker shells and/or a smaller number of shells could be produced by smaller base perturbations in the hydrodynamical models. Partial shells (to be further investigated in Sect. 4) could provide a natural way of reconciling the hydrodynamical models with the observations, as the assumption of spherical symmetry is merely a consequence of computational restrictions.

It is, of course, not excluded that one single shell would explain the IRAS observations. This would be close to the solitary density waves suggested by Waldron et al. (1994) to explain the DACs. In this model a shell is injected into the wind by some unknown mechanism and travels through the wind as a stable wave. This model has been criticised by Owocki (1994a) for the fact that the acceleration is simply derived from a standard β law. More detailed calculations showed the structure resulting from shell-injection in a time-dependent model to be a lot more complex than what Waldron et al. suggest (Owocki et al. 1994).

In principle, it is possible to discriminate between the single shell picture and the multiple shell picture by looking for variability of the infrared flux. The full lines in Fig. 2 can be seen as the time variation of the effect of a single shell travelling outward. Observing at a certain wavelength, we would see the effect appear as the shell enters the formation region

and then disappear again as it moves further out. On the other hand, we would not expect to see much variation if at any given time there are many shells in the formation region. We plan to perform these observations in the near future.

We have also modelled the shells needed to explain the other stars for which the observations could not be explained by a smooth wind (Table 2). For those stars for which we could put constraints on the shell position and strength, we find values in the range of what the time-dependent hydrodynamical models predict. The stars for which clumping is possible (but not always likely) range from O 4 to B 0.5 in spectral type, and are all supergiants. It is not clear whether this is a prerequisite for clumping or simply an observational bias.

In view of the general similarity of these results to those of ζ Pup, we also expect the clumping for these stars to be less (in strength, number or solid angle) than the time-dependent models predict.

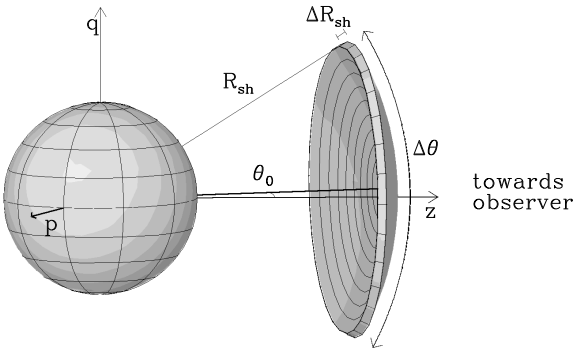

Fig. 5. The geometry of a single *partial* shell. The figure shows a side-view of the situation and defines the (p, q, z) coordinate grid as well as the various parameters of the partial shell ($R_{\rm sh}$, $\Delta R_{\rm sh}$, θ_0 and $\Delta\theta$)

4. Partial shells

4.1. Numerical model

In this section, we expand on the third possibility of reconciling the time-dependent hydrodynamical models and the observations by considering "partial" shells (solid angle $< 4\pi$), possibly alternating with parts of the wind which are smooth (i.e. show no density contrasts). Up to now, theoretical time-dependent hydrodynamical models of instabilities in the stellar wind have, due to computational restrictions, always assumed spherical symmetry. The line drag effect discovered by Lucy (1984) would tend to damp possible lateral instabilities (Rybicki et al. 1990): these therefore would not break up a complete shell, assuming one existed in the first place. However, the recurrence of DACs strongly suggests azimuthal perturbations at the base of the wind. If these are strong enough the lateral instabilities could grow non-linearly and break up the shells (Feldmeier 1995). The lateral scale of these partial shells is difficult to estimate (Owocki 1994a), so we shall not attempt to constrain them a priori.

In the model, we consider a single shell at a position $R_{\rm sh}$ and having a width $\Delta R_{\rm sh}$. We further assume that the partial shell is limited in geometry to angles $\Delta\theta$ around a reference direction which makes an angle θ_0 with the line of sight to the observer (see Fig. 5). The resulting volume is the intersection of a shell and a cone. The solid angle which corresponds to a covering angle $\Delta\theta$ can be found from:

$$\omega = 2\pi \left(1 - \cos\frac{\Delta\theta}{2}\right). \tag{9}$$

Outside the shell the density is given by the smooth wind. Inside the shell the density follows the parabolic density law given by Eq. (1). As usual, values for $\Delta R_{\rm sh}$ are in units of R_* and $\rho_{\rm sh}/\rho_0$ is unitless.

The ionization and excitation in the wind are calculated in the same pseudo-NLTE approach as in Sect. 2.1. The equation of radiative transfer is then solved using a Hubeny model as a lower boundary and including opacities due to hydrogen and helium. In the calculation of the flux from the stellar wind with a partial shell we neglect, for reasons of computational efficiency, the effect of electron scattering. Trial computations in a smooth wind show that neglecting electron scattering reduces the flux by a constant amount of $\sim$ 7 % in the infrared. In the radio region no effect is seen. As we are interested in *differential* effects on the flux (smooth wind vs. clumped wind), neglecting electron scattering will be of little consequence.

The source function at each point is therefore given by the Planck function at the local temperature ($T_{\rm w}$). As usual, we assume that the shell material is at the same temperature as the smooth wind material. For a ray which does not cross the shell, the emergent intensity is the same as for a smooth wind. For rays that do cross the shell, we solve the equations of radiative transfer to get both the intensity with ($I_{\rm em,sh}$) and the intensity without a shell ($I_{\rm em,smooth}$). The emergent intensity calculation uses the formal integral which is solved using a trapezoidal method.

Because of the lack of spherical symmetry, *two* impact parameters (p, q) are needed to describe the position of one ray. For each ray the z-values over which τ and $I_{\rm em}$ are integrated are derived from the intersection of the ray with the fixed radius grid. This radius grid has a higher density of points where large changes in mass density can happen. A sufficiently dense grid of (p, q) integration points is chosen that covers the projected surface area of the shell. The (astrophysical) flux at a distance D can then be derived from:

$$F_{\rm sh} = F_{\rm smooth} + \frac{1}{\pi D^2}\int\int_{\boldsymbol{S}} {\rm d}p{\rm d}q(I_{\rm em,sh} - I_{\rm em,smooth}) \tag{10}$$

where $F_{\rm smooth}$ is the flux due to the smooth wind, $F_{\rm sh}$ the flux due to the wind containing the shell, and $\boldsymbol{S}$ is the cross-sectional area of the partial shell, i.e. its projection on the (p, q)-plane. For notational simplicity the parameters λ, p and q have been dropped. The (z, p)-plane (defined by the reference direction of the shell and the line of sight to the observer) is a plane of symmetry. We therefore need only to calculate one half of the rays covering the shell. A trapezoidal method is used for the

integration to determine the flux. Equation (10) shows that the differential effect on the flux depends on the cross-sectional area of the shell. Cool material in front of the stellar surface can absorb part of the radiation, giving rise to an effect < 1.0.

A trough which has the same covering angle ($\Delta\theta$) as the shell can in principle be included in these calculations. Limiting the covering angle of the trough in this way reflects the basic idea that the partial shell consists of material which has been swept up radially.

In an *isothermal* wind the effect of a shell at θ_0 or $180^\circ - \theta_0$ is nearly the same because the emergent intensity depends only on the source function (which here is assumed constant in the wind) and the total optical depth along the ray (where it is not important at which geometrical depth the effect of the shell is added). The only difference between a θ_0 and $180^\circ - \theta_0$ shell that can exist is due to the possible (complete or partial) occultation by the star.

If furthermore the intensity emitted by the star (I_0) is a Planck function with the same temperature as the wind, then we have that $I_{\rm em} = S = I_0$ for a ray crossing the surface of the star. This is of course nothing else than the Schuster (1905) mechanism.

In this case we have exact equality between a θ_0 and a $180^\circ - \theta_0$ shell. Our models are not isothermal, but the difference between a θ_0 and a $180^\circ - \theta_0$ shell is still small. We therefore restrict our attention to shells with $0^\circ \leq \theta_0 \leq 90^\circ$.

4.2. Application to HD 66811 (ζ Pup, O 4 If)

We apply the partial shell model to ζ Pup, as it is the only star where we have infrared observations up to 60 μm. In this section we concentrate exclusively on the IRAS wavelengths (12, 25 and 60 μm). The parameters of the additional shell (or shells) needed to explain the 1.3 mm flux are not well-constrained, a situation which would not improve with the partial shell model.

The assumption of partial shells also increases the number of parameters. This means that one should not hope to derive a unique solution from the observations. At most we can check whether solutions exist where the physical parameters of the shells are similar to those calculated by Owocki and collaborators (Owocki et al. 1988; Owocki 1992, 1994a) and Feldmeier (1995), except of course for the assumption of spherical symmetry.

We calculated a grid of models for a *single* partial shell, covering a range of shell positions ($R_{\rm sh}$), width ($\Delta R_{\rm sh}$), density contrast ($\rho_{\rm sh}/\rho_0$), covering angle ($\Delta\theta$) and position angle (θ_0). The existence of a trough has little influence on the emergent flux (Sect. 2.1) but severely constrains the spacing of shells. Therefore troughs are not included in the model grid calculations, but they do play an important role in the discussion. For each model we made figures similar to Fig. 4 and determined the best-fit shell parameters. The central points (as defined in Sect. 3) of these fits are summarized in Fig. 6.

The close grouping of the results with different $\Delta R_{\rm sh}$ values indicates that the combination of $\Delta R_{\rm sh}$ and $\rho_{\rm sh}/\rho_0$ into a single shell strength $f_{\rm sh}$ is also appropriate for partial shells. The figure shows that, in order to explain the IRAS fluxes, the shell strength has to increase a lot to compensate for a smaller covering angle. The shell also has to be further away from the stellar surface. The position angle (θ_0) has only a relatively minor effect. For covering angles $\lesssim 90^\circ$, the shell strength for a single shell is no longer in the range of values predicted by Owocki and Feldmeier.

A better limit on the covering angle can be derived by starting from a specific Owocki or Feldmeier model. We then try to see if reducing the solid angle subtended by their shells can explain the IRAS observations, while of course maintaining their shell strength. We shall use the "equivalence" of n shells with a density contrast $\rho_{\rm sub}/\rho_0$ and a width $\Delta\ R_{\rm sub}$ with a single shell of strength $f_{\rm sh}$ given by Eq. (7). The formation region for the IRAS wavelengths is $1 - 7R_*$ (Table 1). Fig. 12 of Feldmeier (1995) shows some 15 shells with an average $\rho_{\rm sh}/\rho_0 \approx 25$ and an average $\Delta R_{\rm sh} \approx 0.05$ within this region. This leads to an equivalent single shell with $f_{\rm sh} \approx 20$ (a more refined calculation not taking averages leads to very much the same result). Fig. 6 shows that a $\Delta\theta = 360^\circ$ shell with $f_{\rm sh} = 20$ does not explain the observations, a conclusion which is of course consistent with the discussion in Sect. 3. If we assume each Owocki and Feldmeier shell to be limited in covering angle to $\Delta\theta = 180^\circ$ we see that the equivalent single shell with $f_{\rm sh} = 20$ can marginally explain the observations. A covering angle of 90° on the other hand already requires a higher $f_{\rm sh}$ value. A covering angle between 90° to 180° would therefore provide a good result: as an average we propose $\Delta\theta = 135^\circ$, corresponding to a solid angle of $\sim 4\pi/3$. If the solid angle covered by each shell is thus reduced, the time-dependent hydrodynamical models can explain the ζ Pup IRAS observations.

The exact limit for this solid angle might change if we split up the single partial shell into smaller partial shell fragments that add up to the same solid angle. The effect on the flux does not change much however, even if we spread the fragments out over a wide range in position angle. This is to be expected from the integrated nature of the infrared emission and is also confirmed by the small effect of θ_0 on Fig. 6. However, if the fragments are at different positions the observed discrepancies might be explained by shells with a *lower* shell strength than for a single partial shell with the same solid angle. In that case the points on Fig. 6 (for $\Delta\theta < 360^\circ$) would be lowered and therefore the value for the limiting solid angle would be lower than $4\pi/3$.

We can estimate by how much the shell strength is lowered: if we assume the fragments to be non-overlapping (as seen by the observer) their differential effects on the flux ($F_{\rm sh}/F_{\rm smooth} - 1$) can simply be added [Eq. (10)]. To save computing time we do not calculate new models for such a fragmented shell, but instead assemble a shell from previously calculated models with smaller covering angle (which represent the fragments). The total covering angle can be derived from the sum of solid angles, where the solid angle of a single shell is given by Eq. (9). Let us consider in this way combinations of three fragments (a larger number of smaller fragments can be combined by repeatedly applying this assemblage).

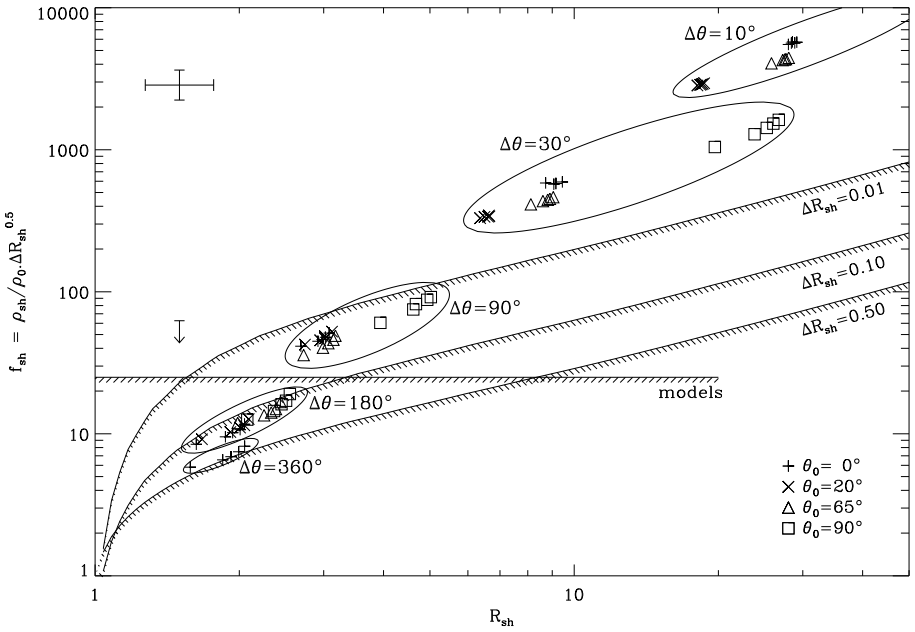

Fig. 6. The results of fitting a *single partial* shell to the *infrared* discrepancies of ζ Pup. Each symbol indicates the best fit solution ($R_{\rm sh}$ and $f_{\rm sh}$) for a given $\Delta R_{\rm sh}$, $\Delta\theta$ and θ_0. $R_{\rm sh}$ and $\Delta R_{\rm sh}$ are expressed in units of R_* and $\rho_{\rm sh}/\rho_0$ is unitless. *No trough* is included in these calculations. The ellipses group results with the same $\Delta\theta$. Within an ellipse, groups of the same symbol indicate the range of $\Delta R_{\rm sh}$ used. Note that the results with different $\Delta R_{\rm sh}$ lie close to one another showing that there is no problem combining $\rho_{\rm sh}/\rho_0$ and $\Delta R_{\rm sh}$ into the single shell strength parameter $f_{\rm sh}$. A typical error bar is given in the upper left corner. The downward pointing arrow shows the maximum value by which the combination of multiple non-overlapping shells can lower the results. The straight hatched line (indicated by "models") gives the upper limit to the shell strengths found in the Owocki and Feldmeier models. The curved hatched lines indicate the upper limit to the area where sufficient material is present on the inside of the shell to create a trough. This dividing line depends on the value of $\Delta R_{\rm sh}$ used and therefore three values have been given

We consider all possible combinations from our grid, thus covering a wide range in differences between the strengths and positions of the 3 shells. We then limit ourselves to those combinations that can explain the observed discrepancies at 12, 25 and 60 μm (within the error bars). Doing so, we find e.g. that 3 shells positioned at slightly different distances, each with $\Delta\theta$ = 90° and θ = 65° can explain the discrepancies. The position angle allows these 3 shells to be placed around the star so they do not overlap from the point of view of the observer. The combined solid angle corresponds to a *single* shell with $\Delta\theta \approx 166°$. The shell strength of a single $\Delta\theta \approx 166°$ shell needed to explain the observations is about 30% higher than the shell strength of the strongest of the 3 shells. This shows how splitting up a single shell (with $\Delta\theta$ = 166°) into three shells (with $\Delta\theta$ = 90°), positioned at slightly different distances, can lower the shell strength required to explain the observations. The example given is actually the worst case we found. The effect decreases rapidly with smaller $\Delta\theta$. Therefore, fragmenting a shell and putting the fragments at different positions will not significantly change the position of the points on Fig. 6. The limiting solid angle of $4\pi/3$ we estimated from the Feldmeier model will therefore not change either.

If we assume the fragments to be totally overlapping, we arrive at a situation as in Sect. 2.2. A large number of weaker fragments can also explain the observations. This is actually the first possible solution we proposed (Sect. 3) to explain the discrepancy between the single shell we found for ζ Pup and the results from the time-dependent hydrodynamical calculations. In this section we concentrate on the third solution (partial shells) and therefore do not further consider the effect of totally overlapping fragments.

The existence of a trough allows us to put further constraints on the single shells presented in Fig. 6. The curved hatched lines indicate the area in the ($R_{\rm sh}$, $f_{\rm sh}$)-plane below which there is sufficient material between the stellar surface and the shell to form a trough. These lines were calculated with the density law derived from the k, α, δ formalism (see Sect 2.1), and assuming that the shell has a rectangular density law as opposed to a parabolic one, and that the density in the trough is zero. The position of this dividing line is dependent on $\Delta R_{\rm sh}$ and three possible values have been shown. One can see that values for the covering angle of 30° or smaller are certainly excluded for the values of $\Delta R_{\rm sh}$ predicted by the Owocki and Feldmeier models, and that the $\Delta\theta$ = 90° shells (corresponding to a solid angle of $4\pi/7$) define the dividing line between models that are possible and those that are not. We therefore take $4\pi/7$ as a firm lower limit on the covering angle. At the same time, this takes into account different possible sources of error.

Using the ideas introduced in this section and in Sect. 2.2, we can in principle study a stochastic form of clumping where

many small clumps (dimensions $\ll$ 1.0 R_*) pervade the smooth stellar wind. Using Eq. (7), the clumps in a certain formation region can be swept up radially into partial shells with the same effect on the flux as the sum of the small clumps. These partial shells can then be seen as a fragmented shell. Thus they are represented by a single partial shell with a total solid angle equal to the sum of the solid angles of the fragments.

5. Discussion

5.1. Uniqueness of the model

We have explained the observed infrared fluxes by the presence of a *single* shell in the stellar wind, with a density contrast comparable to the predictions of time-dependent hydrodynamical models. In these models, however, there are *many* such shells. The available observations do not allow us to tell whether the shell we find represents a physical single shell, or in fact represents the combined effect of a number of shells. Therefore, our results can be interpreted in different ways. It could be that there is truly only one shell in the infrared formation region at a given time. Another possibility is that this region contains a number of shells, weaker than the single shell we found. An observation that could check the single shell interpretation of our results, has been presented in Sect. 3. A third possibility, which allows us to maintain both the strength and the number of shells predicted by the time-dependent hydrodynamical models, is that the shells actually do not fill a complete solid angle. For ζ Pup, we find that the time-dependent hydrodynamical models can explain the observed IRAS fluxes if we assume the shells to be limited to a solid angle of $\sim 4\pi/3$. This solid angle may refer either to the solid angle of the partial shell or to the total solid angle of a number of partial shell fragments.

5.2. Effect of shock-heated gas on the infrared continuum

In our calculations, we have assumed the shell to be at the same temperature as the underlying wind. We now consider the influence of this assumption. The time-dependent models of Feldmeier include the energy-equation and predict that shocks heat part of the gas to $\sim 10^6 - 10^7$ K. In the inner part of the wind, where the density is high, cooling is rapid and the high temperature material is confined to a thin layer at the inner side of each dense shell. In the outer part of the wind ($r \gtrsim 5R_*$), the high temperature regions are broader and coincide with the regions of *low* density (Feldmeier 1995, Figs. 10 and 12).

The effect of a high temperature region on the infrared and radio continuum is the result of two competing effects. The optical depth scales as $T_{\rm w}^{-1.5}$, while the source function (approximated by a Planck function) scales as $T_{\rm w}$ for the wavelengths we consider. Radiative transfer across an optically *thin* shell results in $I_{\rm em} \approx S\Delta\tau \propto T_{\rm w}^{-0.5}$ which means that the flux will go down with higher temperature. This will have to be compensated for by a higher density contrast to explain a given set of observations. As the flux increases as ρ^2, only a slightly higher density contrast will be needed. In optically *thick* cases $I_{\rm em} \approx S \propto T_{\rm w}$, predicting that the flux will increase with higher temperature. Such optically thick cases can occur for shells close to the stellar surface with high density contrast. As shown in Sect. 2.3, for very high density contrast the flux scales as $(R_{\rm sh} + \Delta R_{\rm sh})^2/R_*^2 \times B(\lambda, T_{\rm sh})/B(\lambda, T_*)$. An increase in the shell temperature will allow higher flux values to be attained. This will shift the vertical asymptote in Fig. 4 to lower $R_{\rm sh}$.

We calculated some simplified (Wright and Barlow type) models for a narrow ($10^{-3} - 10^{-2} R_*$) high temperature region ($T = 4 \times 10^6$ K) on the inner side of a complete shell. We found that the cool, outer part of the shell effectively shields the high temperature region, so no effect on the flux is seen. This conclusion is no longer valid when the dimension of the high temperature region becomes comparable to the shell. Somewhat higher $f_{\rm sh}$ values would then be needed to explain the observations (in Fig. 4). If we assume a shell with a thickness of $0.1R_*$, the inner $0.05R_*$ of which is at $T = 4 \times 10^6$ K, this shifts the value of $f_{\rm sh}$ upward by some 30 %. The vertical asymptote in Fig. 4 shifts to the left, thereby lowering the $R_{\rm sh}$ value. The Wright and Barlow type models are too crude to derive a quantitative estimate on the shift of $R_{\rm sh}$.

As for *partial* shells, we see that large ones close to the star are as little influenced by a high temperature region as the complete shells are. For the smaller partial shells, which have to be at larger distances to explain the observations (Fig. 6), little effect is expected because there the hot material is sparse. We performed some calculations which confirmed this expectation. In summary, we therefore expect only small quantitative shifts in the results when temperature effects are taken into account.

5.3. Consequences for current $\dot{M}$ determinations

As the radio continuum of O and B stars is used to determine mass loss rates, the existence of shells raises the question what happens as they move out into the radio formation region. A simple estimate can be obtained as follows. We assume that the material from the shell dissipates into the inter-shell region with a velocity equal to the sound velocity of $\sim$ 20 km s^{-1} (which is certainly much larger than the true dissipation velocity). The required time to traverse the inter-shell distance is $\sim$ 4 days, during which the shell itself has moved from 10 to 60 R_*. The real dissipation process will certainly take longer, so the shells will definitely persist into the radio formation region (see Table 1).

We calculated a model containing some 1200 shells (and corresponding troughs), each with $\Delta R_{\rm sh} = 0.3R_*$ and filling the region $1.5 - 900R_*$. To allow for some dissipation of the density contrast we took $\rho_{\rm sh}/\rho_0 = 4$ (details are given in Runacres & Blomme 1997). The results show that, in this case, the flux at radio wavelengths increases by a factor of 2. Using the Wright and Barlow (1975) formula, this converts to a factor 1.7 for the mass loss rate. This means that, if we use a *smooth* wind model to convert the observed radio flux to a mass loss rate while the real wind is clumped, we overestimate $\dot{M}$ by a factor 1.7. Our results for ζ Pup, however, show that the Owocki and Feldmeier models predict too many shells, suggesting that the shells are partial. The persistence to large distances of such partial shells will

have less influence on the radio emission. Therefore correction factors smaller than 1.7 would need to be applied and, at least for ζ Pup, the radio mass loss rate should be fairly accurate.

Another common way of determining the mass loss rates of early-type stars is from the equivalent width of the Hα emission line. As this is a recombination line it depends on the square of the density and hence is also sensitive to clumping. Lamers and Leitherer (1993) found that the mass loss rates derived from Hα agree well with the radio mass loss rates. Together with the small effect of clumping on the radio flux of ζ Pup, this suggests that the influence of clumping on Hα must also be small. As the Hα line is formed close to the surface of the star (below 1.5 R_*, see Petrenz & Puls 1996) this suggests that clumping might be weak in the innermost part of the wind. This is also what is predicted by the hydrodynamical models, providing that the perturbation at the base of the wind is not too strong.

5.4. Alternative explanations

Up to now we have attributed the IRAS discrepancies exclusively to shells. Additional phenomena (such as wind-compressed zones or co-rotating interaction regions) may play a role. Following on the work of Bjorkmann & Cassinelli (1993), Petrenz & Puls (1996) showed the importance of a wind-compressed zone for the line formation of Hα. As some of the infrared continuum is formed in the same geometrical region, it is in principle possible that the discrepancies found in Paper I can be explained by the ρ^2-effect they found. The wind-compressed zone is not expected to extend so far that it can explain the millimetre discrepancy.

A rough estimate of the effect of a wind-compressed zone can be derived as follows. We approximate the zone by a shell with a covering angle of 90° (a larger angle could hardly be called a "zone"). From Fig. 6 we see that this requires a shell strength of $\sim$ 50. We further use the result of Harries & Howarth (1996) who found a density contrast of at least 1.3. Putting these two numbers into Eq. (6) we find a thickness for the zone of $\sim$ 1500 R_*. Clearly this is a physically unacceptable value: rotation is unlikely to have an effect that far out in the wind. Although a wind-compressed zone cannot account for the entire discrepancy, some contribution is of course possible.

Cranmer & Owocki (1996) present hydrodynamical simulations of co-rotating interaction regions (CIRs). In their models, these are caused by a bright or dark spot on the stellar surface, but they could just as well be generated by magnetic fields or non-radial pulsations. A density contrast is thus created in the wind material and shocks can be formed as well. The CIR creates a structure in the wind which is in some ways similar to the shells we have studied. Density contrast can go up to $\sim$ 50, depending mostly on the contrast of the spot on the stellar surface. Contrary to the shells we studied, this structure turns spirally around the star, extending from the stellar surface up to a few tens of stellar radii. A high density region is followed by a low density trough. It seems impossible to differentiate between (complete or partial) shells which are arranged in a spherically symmetric way around a star, and those in the form of a spiral, as the infrared flux seen by the observer is the result of an integration over a large volume around the star. CIRs with the right density contrast could explain the observations equally well.

Due to its large scale structure the CIR creates variability in the *absorption* part of ultraviolet P Cygni profiles (seen as DACs) when part of the CIR passes between the star and the observer. This variability (and its correlation with the rotation period) is not expected to be observable in the infrared continuum *emission* as almost all the CIR material contributes to the flux. Close to the stellar surface some effect of occultation could, in principle, be seen. However this would have to be searched for at small infrared wavelengths where the flux is dominated by the photosphere. A differentiation between the effect of CIRs and shells caused by the instability of the wind will therefore require results from other observational material than the infrared continuum data alone.

6. Conclusions and future work

As shown in Paper I, a smooth wind model cannot explain the infrared and millimetre observations for *some* O and early B stars. In the present paper we explained these discrepancies by shells, predicted to exist by time-dependent hydrodynamical calculations. We found that the position, strength and number of shells can be derived for sufficiently well-observed stars. The values for the theoretical predictions cannot all agree with the observations. The position of the shell is largely determined by the size of the discrepancies and the wavelengths at which they occur. For the other parameters, there are three possibilities:

- the shells are weaker than predicted
- they have the right strength, but there are less of them
- both the strength and number of shells agree with the predictions, but the shells do not fill a complete solid angle.

Studying the variability of the infrared continuum would be a possible way of discriminating between the first two possibilities. The last solution is appealing in that it maintains the strength and number of shells but relaxes the assumption of one-dimensionality, which is solely a consequence of computational limitations. We find that shells reduced to a solid angle of $\sim 4\pi/3$ explain the IRAS observations of ζ Pup.

The shells persist into the radio formation region and thus increase the radio flux. Therefore mass loss rates derived from radio fluxes using a *smooth* wind model will be overestimated. However, as the ζ Pup IRAS observations can only be explained by weak or partial shells, the effect on the radio flux will be small. Hence, the mass loss rate of ζ Pup derived from radio observations should be reliable.

Although the existence of shells is an obvious hypothesis, co-rotating interaction regions remain a valid alternative. The present infrared data do not allow us to distinguish between CIRs and shells. Continuum variability due to CIRs would be hard to detect as it has to be searched for at near infrared wavelengths, where the flux is dominated by the photosphere.

Wolf-Rayet stars seem to show a more stochastic form of clumping. The density enhancements have a much smaller dimension than the (partial) shells studied here. As explained in

Sect. 4.2, the present model can still be used for this type of clumping, which in principle allows us to study clumping in Wolf-Rayet stars as well.

It is quite clear that infrared continuum observations at wavelengths larger than those covered by IRAS (which are effectively 12 and 25 μm for early-type stars) will provide additional information about material further out in the wind. Because the position of the shell is related to the wavelength at which the maximum effect is reached, one can hope to scan the entire wind. To that end we (with co-investigators K. Vyverman, M. Cohen, C. Leitherer and S. Owocki) have obtained observing time at the Infrared Space Observatory to study a few stars at 60, 90 and 160 μm. The targets to be observed include O and B stars, Wolf-Rayet stars and a Luminous Blue Variable.

Acknowledgements. M.C.R. carried out this research in the framework of the project *Service Centres and Research Networks*, initiated and financed by the *Belgian Federal Scientific Services (DWTC/SSTC)*. We thank S. Owocki and H. Lamers for useful comments. The calculations were performed on the Cray J916 machines of the *Groepering Ruimte/Groupement Espace* and of the Computing Centre of the *Vrije Universiteit Brussel/Université Libre de Bruxelles*.

Appendix A: determination of $\lambda_{\max}$

We are interested specifically in where we have to position the complete shell ($R_{\rm sh}$) to get the maximum differential effect on the flux at a certain wavelength $\lambda_{\max}$. A first estimate for this relation can be found as follows. Along each impact parameter p we can calculate the total optical depth in the wind ($\tau_{\rm max,sh}$), which consists of two parts: the total optical depth in the *smooth* wind ($\tau_{\rm max,smooth}$) and the additional effect due to the *shell* ($\tau_{\rm add}$). Close to the surface of the star there is saturation ($I_{\rm em}/I_{\rm em}(p=0) = 1 - \exp(-\tau_{\rm max,smooth}) \approx 1$), so if we were to position the shell there, very little effect would be seen. Far out in the wind the total optical depth $\tau_{\rm max,smooth}$ is very small and adding $\tau_{\rm add}$ to it would also have little effect. The maximum effect will be reached when we position $R_{\rm sh}$ so that the difference Δ between $1-\exp(-\tau_{\rm max,sh})$ and $1-\exp(-\tau_{\rm max,smooth})$ is largest. To avoid complications due to integration over p, we evaluate Δ at $p = R_{\rm sh}$. We then find:

$$\Delta = -\exp(-\tau_{\rm max,smooth})(\exp(-\tau_{\rm add}) - 1) \tag{A1}$$

where:

$$\tau_{\rm max,smooth}(\lambda, p = R_{\rm sh}) = \int_{-\infty}^{+\infty} \frac{K\gamma A^2}{r^4}\,{\rm d}z = \frac{K\gamma A^2}{R_{\rm sh}^3}\frac{\pi}{2} \tag{A2}$$

and

$$\begin{aligned}\tau_{\rm add}(\lambda, p = R_{\rm sh}) &= 2\int_0^{\sqrt{(R_{\rm sh}+\Delta R_{\rm sh})^2 - R_{\rm sh}^2}} \frac{K\gamma A^2}{r^4}\left(\left(\frac{\rho_{\rm sh}}{\rho_0}\right)^2 - 1\right){\rm d}z \\ &= \frac{K\gamma A^2}{R_{\rm sh}^3}\left(\left(\frac{\rho_{\rm sh}}{\rho_0}\right)^2 - 1\right) G(R_{\rm sh}).\end{aligned} \tag{A3}$$

The geometric factor $G(R_{\rm sh})$ is given by:

$$G(R_{\rm sh}) = \left\{ \arctan\sqrt{\left(\frac{R_{\rm sh}+\Delta R_{\rm sh}}{R_{\rm sh}}\right)^2 - 1} + \left(\frac{R_{\rm sh}}{R_{\rm sh}+\Delta R_{\rm sh}}\right)^2 \sqrt{\left(\frac{R_{\rm sh}+\Delta R_{\rm sh}}{R_{\rm sh}}\right)^2 - 1} \right\}. \tag{A4}$$

The maximum is found at the value of $K(\lambda, T)$ where $\partial\Delta/\partial K = 0$. After some calculation, this gives:

$$K_{\max} = \frac{\ln\left\{1 + 2\left(\left(\rho_{\rm sh}/\rho_0\right)^2 - 1\right) G(R_{\rm sh})/\pi\right\}}{\left(\left(\rho_{\rm sh}/\rho_0\right)^2 - 1\right)\gamma A^2 G(R_{\rm sh})/R_{\rm sh}^3}. \tag{A5}$$

The value of $K_{\max}$ thus found can be converted into a wavelength $\lambda_{\max}$ by using the Rayleigh-Jeans approximation in Eq. (4):

$$\lambda_{\max}^2 = \frac{K_{\max}(\lambda, T_{\rm w}) k T_{\rm w}^{1.5} c^2}{3.7\times 10^8 h Z^2 g(\lambda_{\max}, T_{\rm w})}. \tag{A6}$$

As the Gaunt factor is only a slowly varying function of λ, the above equations allow us to calculate at what wavelength we see the maximum differential effect of a shell at a given distance $R_{\rm sh}$ and with given density contrast $\rho_{\rm sh}/\rho_0$. Inversely, Eqs. (A4), (A5) and (A6) can be used to derive the position of the shell if $\lambda_{\max}$, $\rho_{\rm sh}/\rho_0$ and $\Delta R_{\rm sh}$ are prespecified. Numerical techniques need to be applied for the inversion. Although Eq. (A4) contains $\Delta R_{\rm sh}$, the full effect of $\Delta R_{\rm sh}$ is not included because of the simplifying assumption we made in evaluating Δ at $p = R_{\rm sh}$ [Eq. (A1)]. The formula therefore has only limited accuracy. Contrary to the value of the maximum effect, $\lambda_{\max}$ *does* depend on $\dot{M}$, v_∞ etc.

References

Abbott D.C., Telesco C.M., Wolff S.C. 1984a, ApJ 279, 225
Abbott D.C., Bieging J.H., Churchwell E., 1984b, ApJ 280, 671
Beichman C.A., Neugebauer G., Habing H.J., Clegg P.E., Chester T.J., 1988, Infrared Astronomical Satellite (IRAS). Catalogs and Atlases. NASA Reference Publication 1190
Berghöfer T.W., Schmitt J.H.M.M., 1994, A&A 290, 435
Berghöfer T.W., Baade D., Schmitt J.H.M.M., et al., 1996, A&A 306, 899
Bieging J.H., Abbott D.C., Churchwell E.B., 1989, ApJ 340, 518
Bjorkmann J.E., Cassinelli J.P., 1993, ApJ 409, 429
Blomme R., 1990, A&A 229, 513
Bunn J.C., Drew J.E., 1992, MNRAS 255, 449
Cassinelli J.P., Hartmann L., Sanders W.T., Dupree A.K., Myers R.V., 1983, ApJ 268, 205
Cassinelli J.P., Cohen D.H., MacFarlane J.J., Sanders W.T., Welsh B.Y., 1994, ApJ 421, 705
Castor J.I., Simon T., 1983, ApJ 265, 304
Castor J.I., Abbott D.C., Klein R.I., 1975, ApJ 195, 157
Chlebowski T., 1989, ApJ 342, 1091
Collura A., Sciortino S., Serio S., et al., 1989, ApJ 338, 296
Conti P.S., Frost S.A., 1977, ApJ 212, 728
Cranmer S.R., Owocki S.P., 1996, ApJ 462, 469

Ebbets D., 1980, ApJ 235, 97
Ebbets D., 1981, PASP 93, 119
Ebbets D., 1982, ApJS 48, 399
Feldmeier A., 1995, A&A 299, 523
Groenewegen M.A.T., Lamers H.J.G.L.M., 1989, A&AS 79, 359
Groenewegen M.A.T., Lamers H.J.G.L.M., Pauldrach A.W.A., 1989, A&A 221, 78
Harries T.J., Howarth I.D., 1996, A&A 310, 533
Hillier D.J., Kudritzki R.P., Pauldrach A.W., et al., 1993, A&A 276, 117
Hubeny I., 1988, Comp. Phys. Comm. 52, 103
Kaper L., Henrichs H.F., Nichols J.S., et al., 1996, A&AS 116, 257
Lamers H.J.G.L.M., Leitherer C., 1993, ApJ 412, 771
Lamers H.J.G.L.M., Waters L.B.F.M., 1984, A&A 138, 25
Lamers H.J.G.L.M., Waters L.B.F.M., Wesselius P.R., 1984, A&A 134, L17
Lamers H.J.G.L.M., Snow T.P., De Jager C., Langerwerf A., 1988, ApJ 325, 342
Leitherer C., Robert C., 1991, ApJ 377, 629
Lucy L.B., 1982, ApJ 255, 278
Lucy L.B., 1983, ApJ 274, 372
Lucy L.B., 1984, ApJ 284, 351
Lucy L.B., Solomon P.M., 1970, ApJ 159, 879
MacFarlane J.J., Waldron W.L., Corcoran M.F., et al., 1993, ApJ 419, 813
Moffat A.F.J., Michaud G., 1981, ApJ 251, 133
Mullan D.J., 1984, ApJ 283, 303
Mullan D.J., 1986, A&A 165, 157
Olson G.L., Ebbets D., 1981, ApJ 248, 1021
Owocki S.P., 1992, in: Heber U., Jeffery S. (eds.) The Atmospheres of Early-Type Stars. Springer-Verlag, Heidelberg, p. 393
Owocki S.P., 1994a, ApSS 221, 3
Owocki S.P., 1994b, ApSS 221, 491
Owocki S.P., Rybicki G.B., 1984, ApJ 284, 337
Owocki S.P., Rybicki G.B., 1985, ApJ 299, 265
Owocki S.P., Rybicki G.B., 1986, ApJ 309, 127
Owocki S.P., Castor J.I., Rybicki G.B., 1988, ApJ 335, 914
Owocki S.P., Fullerton A.W., Puls J., 1994, ApSS 221, 437
Owocki S.P., Cranmer S.R., Gayley K.G., 1996, preprint
Pallavicini R., Golub L., Rosner R., et al., 1981, ApJ 248, 279
Pauldrach A., Puls J., Kudritzki R.P., 1986, A&A 164, 86
Pauldrach A.W.A., Kudritzki R.-P., Puls J., Butler K., Hunsinger J., 1994, A&A 283, 525
Petrenz P., Puls J., 1996, A&A 312, 195
Prinja R.K., 1988, MNRAS 231, 21P
Puls J., Kudritzki R.-P., Herrero A., et al., 1996, A&A 305, 171
Runacres M.C., Blomme R., 1994, ApSS 221, 249
Runacres M.C., Blomme R., 1996, A&A 309, 544 (Paper I)
Runacres M.C., Blomme R., 1997, A&A, submitted
Rusconi L., Sedmak G., Stalio R., Arpigny C., 1980, A&AS 42, 347
Rybicki G.B., Hummer D.G., 1991, A&A 245, 171
Rybicki G.B., Owocki S.P., Castor J.I., 1990, ApJ 349, 274
Schuster A., 1905, ApJ 21, 1
Sciortino S., Vaiana G.S., Harnden F.R. Jr., et al., 1990, ApJ 361, 621
Snow T.P. Jr., Wegner G.A., Kunasz P.B., 1980, ApJ 238, 643
Snow T.P. Jr., Cash W., Grady C.A., 1981, ApJ 244, L19
Waldron W.L., Klein L., Altner B., 1994, ApJ 426, 725
White R.L., 1985, ApJ 289, 236
Wright A.E., Barlow M.J., 1975, MNRAS 170, 41

This article was processed by the author using Springer-Verlag LaTeX A&A style file *L-AA* version 3.